Paleosalinity of the Nanhua Basin (South China) during the Cambrian Explosion

Hongjie Zhang [a,b], Haifeng Fan [a,b,*], Fang Zhang [a,b], Hanjie Wen [b,c]

[a] State Key Laboratory of Ore Deposit Geochemistry, Institute of Geochemistry, Chinese Academy of Sciences, Guiyang 550081, China
[b] University of Chinese Academy of Sciences, Beijing 100049, China
[c] School of Earth Sciences and Resources, Chang'an University, Xi'an 710054, China

ARTICLE INFO

ABSTRACT

Similar to marine oxygen level and nutrient supply, seawater salinity has also been suggested as an important control on marine biological evolution. However, the potential links between the seawater salinity and Cambrian Explosion remain unclear. Here, we conducted high-resolution analyses of B/Ga and B/K ratios on four typical sections from different water-depth environments to constrain the paleosalinity in the Nanhua Basin (South China) from late Age 2 to Age 3 ($\sim$526–515 Ma). Our new data revealed common hypersaline conditions at shallow-water Meishucun (B/Ga = 13.8 $\pm$ 2.3 and B/K = 73.5 $\pm$ 15.7) and Wangjiaping (B/Ga = 20.6 $\pm$ 2.7 and B/K = 101.1 $\pm$ 17.1) locales during most of the period from late Age 2 to Age 3. In contrast, combined with the deep-water data in a recent study, middle- to deep-water environments were dominated by brackish to normal seawater salinity, as documented at Zhijin (B/Ga = 8.0 $\pm$ 1.1 and B/K = 48.2 $\pm$ 4.5), Daotuo (B/Ga = 6.4 $\pm$ 1.6 and B/K = 57.6 $\pm$ 12.3), Yuanjia (B/Ga = 4.3 $\pm$ 2.7), and Zhalagou (B/Ga = 6.1 $\pm$ 1.2) locales. Notably, two transient low-salinity intervals (LS1 and LS2) developed in shallow-water regions at $\sim$526 Ma and $\sim$518 Ma, respectively, because of increased freshwater inputs, during which the watermass salinity may be inhabitable for early faunas. Combined with previous redox studies, however, transient shallow-water anoxia at $\sim$525 Ma allowed only the development of hypoxia-tolerant sponge faunas during LS1, indicating redox constrains on the early biological evolution. Additionally, although studies indicated rapid oceanic oxygenation within the hypersaline interval between LS1 and LS2, no important biotas occurred at this hypersaline interval, indicating hypersalinity restriction on metazoan diversification. Instead, when normal seawater salinity and oxic watermass were jointly formed during LS2 ($\sim$518 Ma), the Chengjiang and Qingjiang biotas experienced notable explosion. Therefore, the influences of the seawater salinity on early life evolution should be given more attention in the future.

1. Introduction

The early Cambrian (Fortunian to Age 3) witnessed a revolutionary radiation of skeletal metazoans known as the Cambrian Explosion, which may have deep roots in the Ediacaran Biota (Shore et al., 2021). The main phase of the Cambrian Explosion is characterized by the Chengjiang and Qingjiang biotas (Fu et al., 2019), the former of which was recently dated to $\sim$518 Ma (Yang et al., 2018). The Cambrian Explosion was a composite consequence of external environments, gene regulatory networks, and ecological effects, in which the changes in the atmosphere and marine environments may have functioned as critical triggers (Reinhard et al., 2017; Hearing et al., 2018; Krause et al., 2018).

Early studies mainly focused on atmospheric and marine oxygen levels and found that atmospheric and oceanic oxygenation may have stimulated the Cambrian Explosion (Krause et al., 2018; Zhuravlev et al., 2022). However, studies also proposed that the Cambrian Explosion was developed in an overall low-oxygen environmental background (Sperling et al., 2015; Hammarlund et al., 2017). Moreover, the early Cambrian biotas mainly inhabited shallow-water environments, where waters were dominated by relatively stable oxic conditions at that time (Li et al., 2017; Guilbaud et al., 2018). These observations may indicate additional environmental factors of the Cambrian Explosion, such as the seawater salinity, temperature, and nutrients (Reinhard et al., 2017; Hearing et al., 2018).

Particularly, early modeling studies found that the seawater salinity may have quickly decreased from hypersaline (saltier than normal seawater) conditions during most of the Precambrian period to near-modern values during the Ediacaran–Cambrian transition (Knauth, 2005; Hay et al., 2006). In fact, salinity fluctuations can significantly influence marine organisms and ecosystems, exposure to hypersaline conditions can result in passive capture of seawater ions across the organism surface owing to an increased osmotic gradient (Henry et al., 2012). This process is fatal to most marine organisms, particularly to those osmoconformers that cannot perform osmotic regulation of their extracellular fluid and rely solely on isosmotic intracellular regulation (Zhang et al., 2021). For example, Winter et al. (1983) found that a sharp salinity increase to hypersaline conditions prior to the Last Glacial Maximum induced a prominent decrease in biological diversity in the Aqaba Gulf and indicated that an ~50‰ salinity may approximate the upper salinity tolerance limit of most planktonic organisms. Similarly, both planktonic and benthic faunal diversity experienced a significant decrease immediately before the late Messinian salinity crisis (Kontakiotis et al., 2022). Also, large burrowing and bioturbating macrofauna are generally absent in modern hypersaline lagoons because they will gradually lose their functional traits following salinity increases (Shadrin et al., 2019; Lam-Gordillo et al., 2022). These observations indicate that salinity conditions are critical to life evolution. However, the detailed paleosalinity evolution and its links to biological diversification during the Cambrian Explosion have not been well constrained, which may be partially attributed to underdeveloped geochemical proxies for the paleosalinity (Wei and Algeo, 2020).

Recently, Wei and Algeo (2020) and Retallack (2020) proposed that the $B_{(ppm)}/Ga_{(ppm)}$ and $B_{(ppm)}/K_{(\%)}$ ratios (the same below) in bulk shales are robust paleosalinity proxies because the B content in clay minerals and clay-enriched sediments is closely related to the salinity of the parent aqueous solution (Frederickson and Reynolds, 1960). Generally, a B/Ga ratio of >6 (Wei and Algeo, 2020) and a B/K ratio of >40 (Retallack, 2020) characterize the marine (salinity = 30–38‰) threshold and distinguish marine facies from fresh (salinity <1‰) and brackish facies (salinity = 1–30‰) based on the modern data compilation. Particularly, the B/Ga ratios of shales and partial carbonates have been widely employed to reconstruct the paleosalinity of ancient oceans or basins. Examples include the early Cambrian Nanhua Basin (middle to deep waters; Cheng et al., 2023), Early Jurassic Northwest European Sea (Remírez and Algeo, 2020), and Late Pennsylvanian North American Midcontinent Sea (Wei et al., 2022). In Cheng et al. (2023), the authors observed a salinity increase in the early Cambrian Nanhua Basin, which has been attributed to an increased connection with the open ocean. They further proposed that this hydrological change may have promoted watermass mixing and oxygenation in the Nanhua Basin and thus facilitated the metazoan evolution (Cheng et al., 2023). However, because of lacking important fossil records in the middle- to deep-water sections, a direct influence of watermass salinity on the Cambrian Explosion remains unclear. On the other hand, Jewuła et al. (2022) suggested that the B/Ga and B/K ratios in sediments are highly sensitive to mineralogical changes during post-depositional alteration. Therefore, it is very important to evaluate the post-depositional effects on the B/Ga and B/K ratios before utilizing them for paleosalinity reconstruction. Nevertheless, the B/Ga and B/K ratios currently provide us with an opportunity to assess paleosalinity links to biological diversification during the Cambrian Explosion.

Early Cambrian sedimentary strata are well documented in the Nanhua Basin, where the Chengjiang (Yunnan Province) and Qingjiang (Hubei Province) biotas representing the main phase of the Cambrian Explosion are well preserved in shallow-water regions (Steiner et al., 2005; Fu et al., 2019). Additionally, the early Cambrian sediments are dominated by black shales in the Nanhua Basin, which are suitable for B-derived paleosalinity reconstruction (Wei and Algeo, 2020), providing an ideal laboratory to explore paleosalinity links to biological evolution during the Cambrian Explosion. Here, we conducted B/Ga and B/K ratio

analyses on four comparative sections from different water-depth environments (shallow to middle waters) in the early Cambrian Nanhua Basin. Combined with the deep-water data in Cheng et al. (2023), we achieved B-derived paleosalinity reconstruction of the Nanhua Basin across the main phase of the Cambrian Explosion from late Age 2 to Age 3 (~526–515 Ma). Combined with sea-level reconstruction results and pyrite $\delta^{34}S_{py}$ values, we discussed the major controls of the paleosalinity evolution at that time and provided critical evidence of salinity control on the Cambrian Explosion.

2. Geological setting

The South China Craton was isolated in the Paleo-Asian Ocean during the Ediacaran–Cambrian transition, in which a failed rift basin (Nanhua Basin) developed between the Yangtze and Cathaysia blocks (Fig. 1). The paleolatitudes of the South China Craton shifted gradually during the Ediacaran–Cambrian transition. Specifically, the paleolatitudes could have shifted from >30°N at ~635 Ma to the paleoequator at ~510 Ma (Zhang et al., 2015). At ~530–515 Ma, the South China Craton was located at ~10–20°N paleolatitudes (Meert and Lieberman, 2008; Zhang et al., 2015). During the early Cambrian, the Nanhua Basin developed systematic shallow-to-deep deposition environments from northwest to southeast in modern coordinates (Fig. 1). From late Age 2 to Age 3, the Nanhua Basin was dominated by shale deposition; examples include the Shuijingtuo and Qiongzhushi formations in shallow-water environments and the Niutitang and Jiumenchong formations in middle to deep waters (Zhu et al., 2003). Here, the shallow-water Qiongzhushi Formation in Meishucun (Yunnan Province) and Shuijingtuo Formation in Wangjiaping (Hubei Province) and the middle-depth water Niutitang Formation in Zhijin and Jiumenchong Formation in Daotuo (Guizhou Province) were studied (Fig. 1).

In Meishucun, the Qiongzhushi Formation comprises the Shiyantou Member and the Yu'anshan Member upwards, which are dominated by black shale with increased siltstone in the upper part of each member (Fig. 2). The Qiongzhushi Formation discontinuously overlies the Zhujiaqing Formation, which is dominated by phosphorites and carbonates (Fig. 2). The Shiyantou Member is poorly fossiliferous, but it contains abundant sponge spicules in the lower part (Steiner et al., 2007). Notably, the Chengjiang Biota was intensively developed in the middle-lower part of the Yu'anshan Member (Hammarlund et al., 2017). A tuff layer in the basal Shiyantou Member was dated to SHRIMP U—Pb ages of 526.5 ± 1.1 Ma (Compston et al., 2008), indicating late Age 2 products. Additionally, the Chengjiang Biota has been proposed to be initiated at 518.03 ± 0.69/0.71 Ma based on CA-ID-TIMS U—Pb dating of detrital zircons (Yang et al., 2018).

In Wangjiaping, the Shuijingtuo Formation discontinuously overlies the Yanjiahe Formation (Fig. 2). The Shuijingtuo Formation is dominated by black shales with increased carbonate and siltstone components in the upper part (Fig. 2). The Qingjiang Biota was intensively exploded in the middle-lower part of the Shuijingtuo Formation (Fu et al., 2019). Additionally, large amounts of sponge fossils also occurred in the basal Shuijingtuo Formation (Liu et al., 2022). A basal tuff layer below a P-nodule layer in the Shuijingtuo Formation was dated to NanoSIMS U—Pb ages of 526.4 ± 5.4 Ma (Okada et al., 2014). Upwards, a Ni—Mo sulfide layer occurs intermediately above the P-nodule layer, the equivalents of which have been dated to 521 ± 5 Ma by the Re—Os system (Xu et al., 2011), which approximates the Age 2–Age 3 boundary. Additionally, the Qingjiang Biota is biologically equivalent to the Yunnan Chengjiang Biota (Fu et al., 2019), indicating basically similar ages of ~518 Ma.

In Zhijin, the black shales of the Niutitang Formation discontinuously overlie the phosphorites of the Gezhongwu Formation (Fig. 2). Large amounts of sponge spicules have been observed in the phosphorites of the Gezhongwu Formation (Yang et al., 2004). A Ni—Mo sulfide layer occurs in the basal Niutitang Formation, which has been dated to 521 ± 5 Ma by Re—Os system (Xu et al., 2011). In Daotuo, the
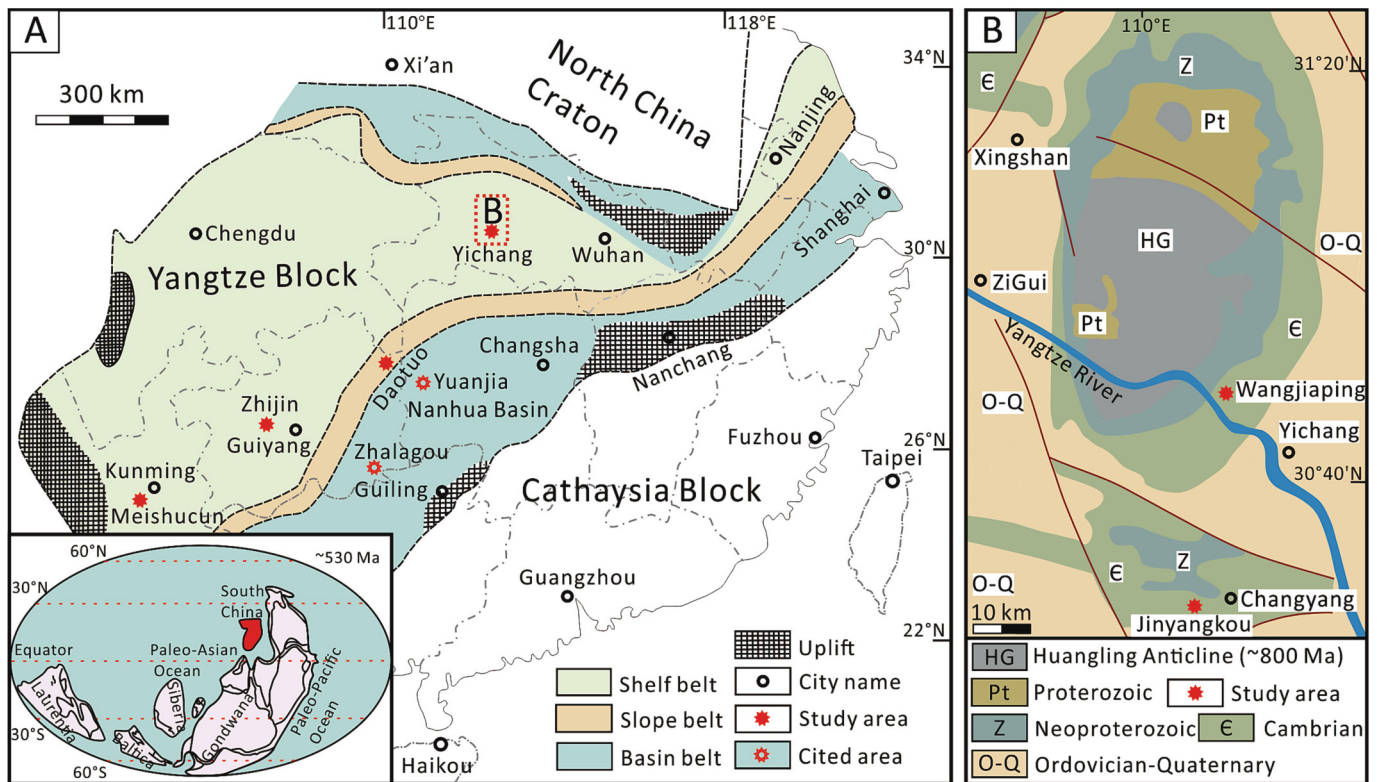
Fig. 1. Early Cambrian paleogeographic map of South China marked with the studied locations (A) and regional geological map of Yichang district in Hubei Province (B) (modified from Jiang et al., 2012). Note that the Jinyangkou locale may be much deeper than the Wangjiaping locale during the early Cambrian given their relative positions to the Neoproterozoic Huangling Anticline.
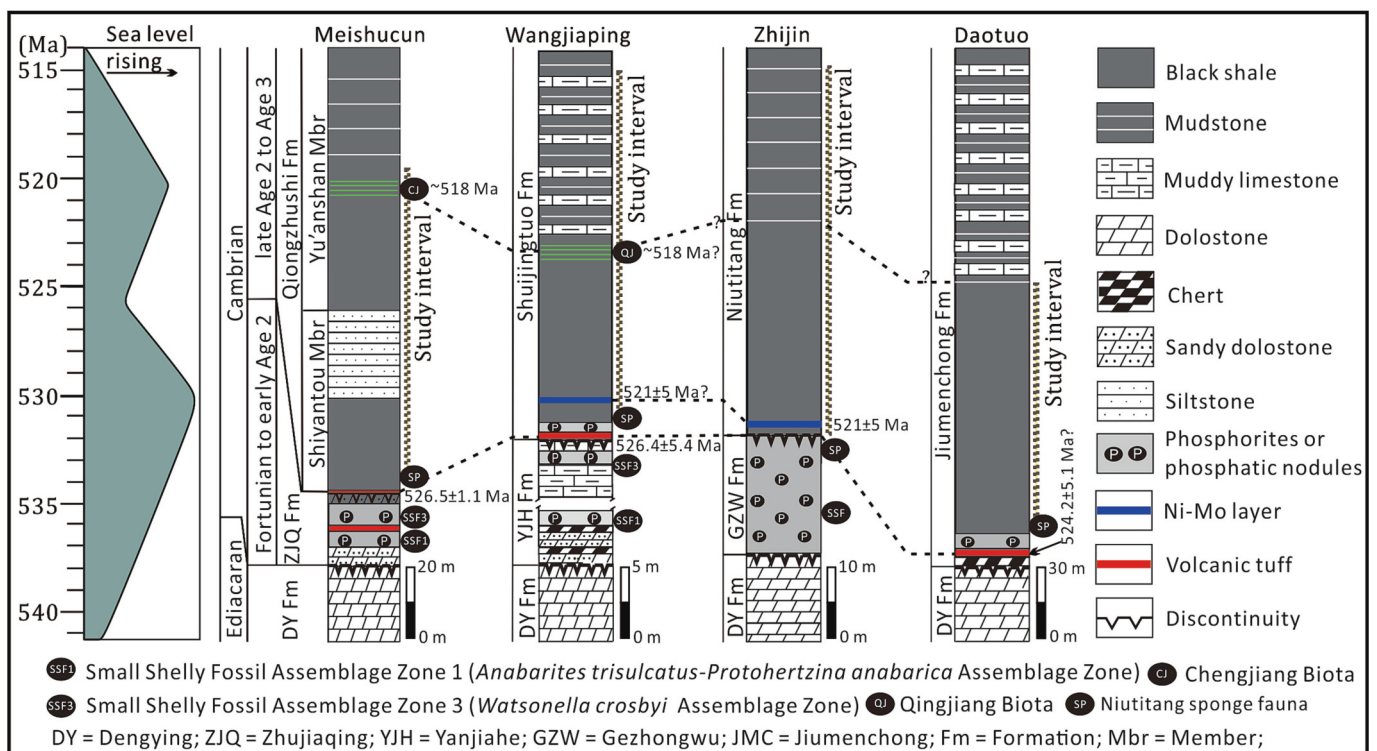

Fig. 2. Stratigraphy and stratigraphic correlations of the studied sections in the Nanhua Basin, South China (marked with the sampling ranges). The chronostratigraphic information of the studied sections was cited from Compston et al. (2008), Xu et al. (2011), Okada et al. (2014), Chen et al. (2015a), and Yang et al. (2018).

Jiumenchong Formation discontinuously overlies the Dengying Formation characterized by carbonates (Fig. 2). The Jiumenchong Formation is dominated by black shales with increased carbonates in the upper part (Fig. 2). A P-nodule layer is developed in the basal Jiumenchong Formation, in which sponge spicules may have occurred (Huang et al., 2019). A volcanic tuff is developed below the P-nodule layer, which has been dated to zircon U—Pb ages of 522.3 ± 3.7 Ma and 524.2 ± 5.1 Ma at nearby (several tens km away) Bahuang and Panmen sections, respectively (Chen et al., 2015a), which also indicate late Age 2 products. A summary of the overall stratigraphic correlations is shown in Fig. 2.

3. Samples and methods

3.1. Samples

In Meishucun, the Shiyantou Member was collected from an outcrop, and the Yu'anshan Member was sampled from a nearby drill-core. In Yichang district, a complete Shuijingtuo Formation was collected from a drill-core near Wangjiaping village (Fig. 1). Also, we collected fossiliferous (Qingjiang Biota) samples from the Shuijingtuo Formation in Jinyangkou (Fig. 1), where the Qingjiang Biota has been reported (Fu et al., 2019). The biota interval is characterized by alternating occurrences of dark background layers and light-gray event layers (Hammarlund et al., 2017; Fu et al., 2019). In addition, the complete Niutitang Formation in Zhijin and the lower Jiumenchong Formation (dominated by shale) in Daotuo were collected from two drill-cores. All bulk samples were first treated with a water-cooled cutting machine to remove any stale surfaces. The fresh remains were then crushed into 200-mesh powders. All subsequent geochemical analyses were conducted on these powders. Representative samples were cut to produce 50–100 μm thick sections for petrographic observation.

3.2. Methods

The mineral compositions of powder samples was identified by using X-ray diffraction (XRD) at the Analysis and Testing Center of the China Three Gorges University. To better constrain the clay-mineral composition, one representative sample was first subjected to clay-mineral purification through water chromatography, after which XRD analysis under air-dried (AD), glycol-saturated (EG), and heated (T) conditions was performed. Detailed principles of the clay mineral identification can be found in Ye et al. (2016). The relative mineral proportion can be evaluated using the peak intensity (semiquantitative in nature). Additionally, polished thin sections were examined by using a TESCAN Intergrated Mineral Analyzer (TIMA) at Guangzhou Tuoyan Analytical Technology Co., Ltd., which comprises a MIRA3 SEM system with four EDS detectors. The liberation mode was employed during TIMA analysis, which included the collection of BSE and EDS data at individual points, which were then grouped based on a similarity search algorithm to produce mineral segments. Data from each segment were then compared to a predefined library to create a mineral map, which was automatically finished by the TIMA system. Detailed principles of the TIMA system can be found in Hrstka et al. (2018).

B and other trace elements were analyzed by using the B-MS82L and ME-MS61r methods, respectively, at ALS Chemex (Guangzhou) Co., Ltd. For B analysis, ~500 mg powder samples were fused with sodium hydroxide in a nickel crucible over a flame to ensure adequate B extraction. The resulting melt was dissolved in deionized water to produce a B solution. Subsequently, the solution was diluted and then measured by ICP-MS. Four laboratory standards (BCS396, GBW07709, OREAS 216b, and OREAS 219) were analyzed together with our samples, which showed that the relative errors were better than 10%. Additionally, ~50 mg powder samples were used for trace element analysis. The powder samples were completely digested by using concentrated mixed acid and then dissolved in 2% HNO_3 for ICP-MS measurement. The analytical

results of two USGS standards (BHVO-2 and BCR-2) suggested that the relative errors were better than 3%.

Pyrite $\delta^{34}S_{py}$ analysis was finished in the State Key Laboratory of Biogeology and Environmental Geology, China University of Geosciences (Wuhan). Major procedures have been detailed in Zhang et al. (2018). Two international standards IAEA S2 ($\delta^{34}S = 22.7‰$) and IAEA S3 ($\delta^{34}S = 32.3‰$) and two national standards GBW04415 ($\delta^{34}S = 22.4‰$) and GBW04414 ($\delta^{34}S = 0.1‰$) were used to monitor the instrument drift, which suggested a precision of better than 0.4‰ (2SD). The $\delta^{34}S_{py}$ values were reported relative to the international standard of Vienna Cañon Diablo Troilite (VCDT).

4. Results and discussion

4.1. Evaluation of the B-derived salinity proxies

B-derived salinity proxies are based on the observations that the B content in aqueous solutions exhibits a linear relationship with the salinity, and this correlation can be accurately documented in clay minerals and clay-enriched sediments, particularly when clay minerals are dominated by illite (Frederickson and Reynolds, 1960; Ye et al., 2016; Wei and Algeo, 2020). Both XRD analysis and TIMA mineral mapping demonstrated that clay minerals are the major mineral components in the studied shales, in which illite was the predominant clay-mineral phase (Figs. 3 and 4). In this situation, we can preliminarily argue that our samples are suitable for B-derived paleosalinity reconstruction. Because the total clay minerals in bulk-rock samples are changeable (Fig. 3), the B content in bulk-rock cannot be employed as a direct paleosalinity proxy. The latest compilations of published data on modern clay-enriched bulk-rock sediments show that the B/Ga and B/K ratios are effective proxies for paleosalinity reconstruction because Ga and K are mainly present in clay minerals and are insensitive to salinity (Retallack, 2020; Wei and Algeo, 2020). The lack of correlations between the Al content and the B/Ga and B/K ratios in the studied shales (Supplementary Fig. S1) also validates that clay content makes negligible effects on bulk-rock B/Ga and B/K ratios. However, a detrital and weathering origin of B and diagenetic and metamorphic alteration can significantly alter the chemical deposition-related B/Ga and B/K ratios in ancient sediments (Moran et al., 1992; Srodon, 2010; Jewuła et al., 2022).

In general, silicate detritus is characterized by a low B content of <10 ppm, and thus, the average upper crust gives extremely low B/Ga (0.9) and B/K (5.4) ratios, respectively (McLennan, 2001). However, the studied samples yielded much higher B/Ga (3.1–25.1) and B/K (33.2–120.9) ratios than detrital signals (Fig. 5), which excludes detritus-dominated control. Additionally, if samples contain abundant K-feldspar and mica, which are typically depleted in B but enriched in K, the B/K ratios can be largely diluted (Walker, 1968; Jewuła et al., 2022). However, only minor K-feldspar and mica were detected during mineralogy observation (Figs. 3 and 4), which cannot significantly affect the B/K ratio. The covaried B/Ga and B/K ratios also indicated that the B/K ratios were not greatly diluted by detrital K-feldspar and mica. On the other hand, weathering processes can significantly elevate the initial B/Ga and B/K ratios because of B enrichment in weathering-originated kaolinite and hematite (Jewuła et al., 2022). However, most of the studied samples were collected from drill-cores, which can greatly prevent weathering influences. Also, only minor kaolinite and no hematite were detected in the studied shales during mineralogy observation (Figs. 3 and 4), which excludes strong weathering effects. Additionally, Ga is much more conservative than K during weathering, resulting in nearly constant Ga/Al ratios and systematically decreasing K/Al ratios in residues (Clift et al., 2014; Richardson et al., 2022). Therefore, strong weathering can produce decoupled B/Ga and B/K ratios with suspiciously high B/K ratios; examples are the paleosol and regolith data reported by Jewuła et al. (2022). The B/Ga and B/K ratios are generally covaried in the studied samples (Fig. 6), indicating again the absence of prominent weathering influences.
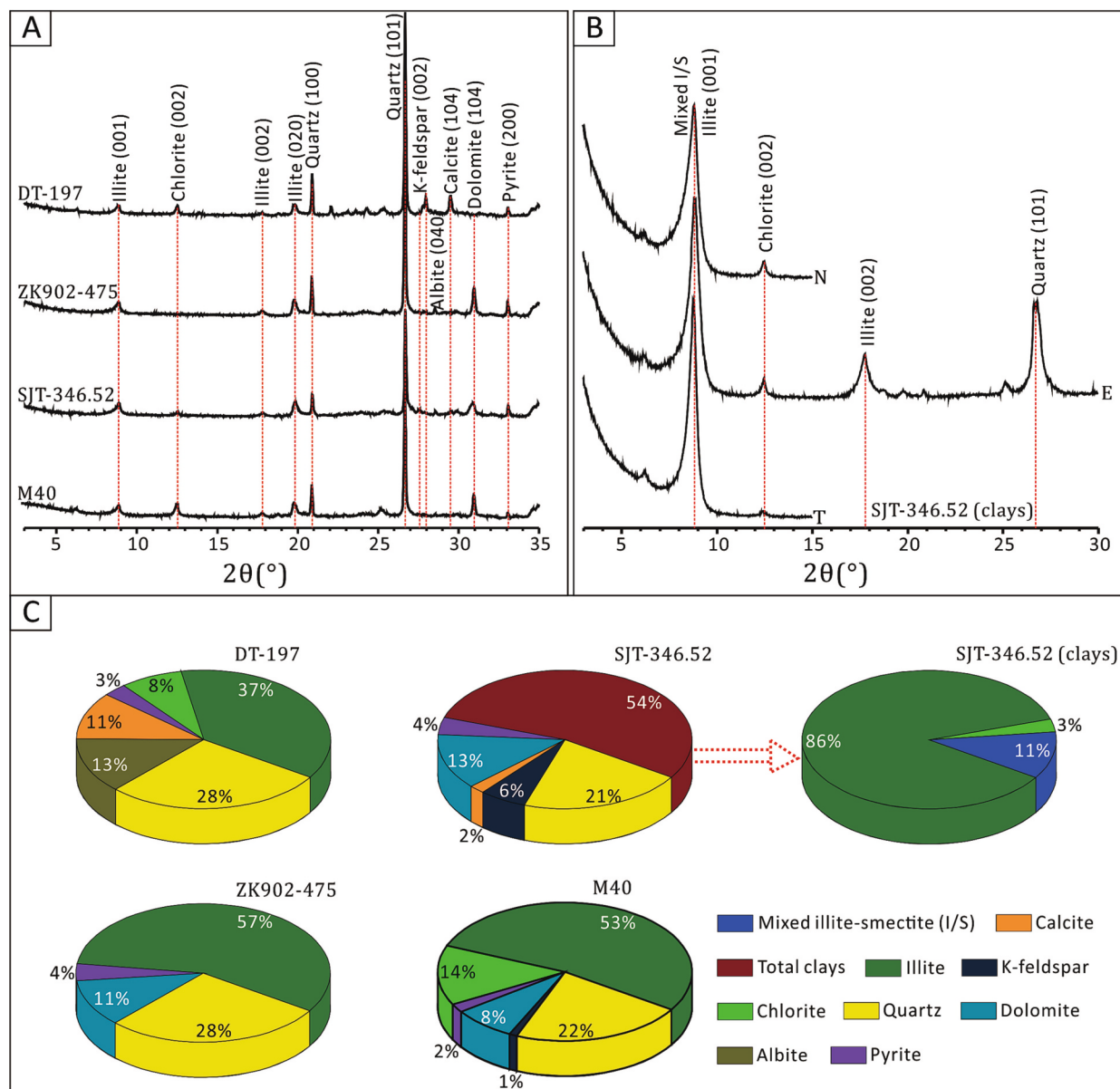
Fig. 3. XRD patterns of four representative bulk samples (A) and one purified clay-mineral sample (B) of the studied sections. The relative mineral content is displayed as a pie chart (C).

Additionally, both diagenetic and metamorphic alterations involve B recycling, which may induce post-depositional B loss or accumulation (Moran et al., 1992; Srodon, 2010; Retallack, 2020). For instance, Srodon (2010) found that diagenetic illitization of unconsolidated pyroclastic bentonite beds can systematically enrich the beds with B possibly released from external organic matter. Another study by Środoń and Paszkowski (2011) instead proposed that diagenetic illitization of shales only involved B redistribution within internal clay minerals without net exchange of B with pore fluids. These observations may indicate that the tightness of shales in deep burial environments generally precludes late-stage B recycling during diagenesis, which has also been mentioned by Wei et al. (2022). Four representative shale samples are all characterized by high illite content (~30–60%; Fig. 3), indicating potential diagenetic illitization. However, although the SJT-346.52, ZK902–475, and M-41 samples have similar illite contents (54%, 57%, and 53%, respectively), they have totally different B/Ga (20.9, 8.9, and 13.4, respectively) and B/K (106.8, 46.2, and 83.8, respectively) ratios. Therefore, the observed B/Ga and B/K variations in our samples cannot be attributed to diagenetic illitization. However, relatively high-temperature metamorphic

processes can induce B loss even in consolidated sediments (Moran et al., 1992; Retallack, 2020), consistent with an experimental observation documenting boron desorption from clays at temperatures higher than 100 °C (You et al., 1995). For example, Retallack (2020) found that any obvious metamorphic alteration will significantly deplete B in sediments, the B/K threshold between marine and non-marine environments can be reduced from 40 in unaltered sediments to 21 under bituminous conditions and to 5 in anchimetamorphic zones (close to the greenschist facies). However, illite dominates the clay-mineral phase in the studied shales (Figs. 3 and 4). In this situation, diagenetic illitization of shales can greatly retain remobilized B, thus minimizing B loss (Środoń and Paszkowski, 2011). As shown in Fig. 5, almost all B/K ratios were higher than the marine threshold identified by modern unaltered sediments (40; Retallack, 2020), indicating negligible metamorphic B loss. Also, regional metamorphic processes would only lower the absolute B/Ga and B/K ratios, and it is impossible to build the systematic evolution in stratigraphic sequences (Fig. 6). Therefore, temporal changes in B-derived proxies are more likely to reflect salinity changes rather than metamorphic loss of B. In conclusion, the B/Ga and B/K ratios in our
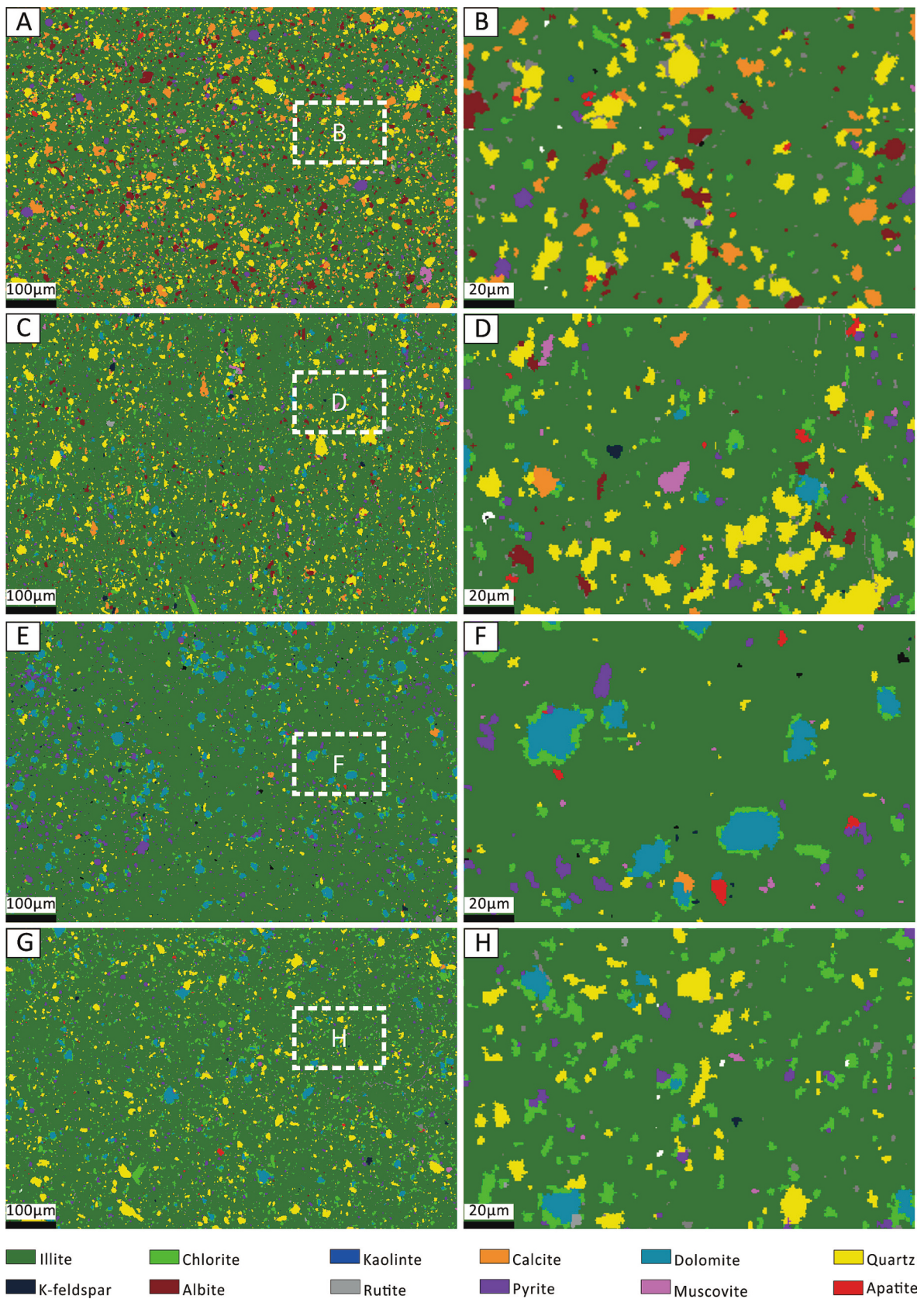
Fig. 4. TIMA mineral mapping of the four representative samples of the studied sections. Note that only >0.1% (in vol.) minerals are displayed.
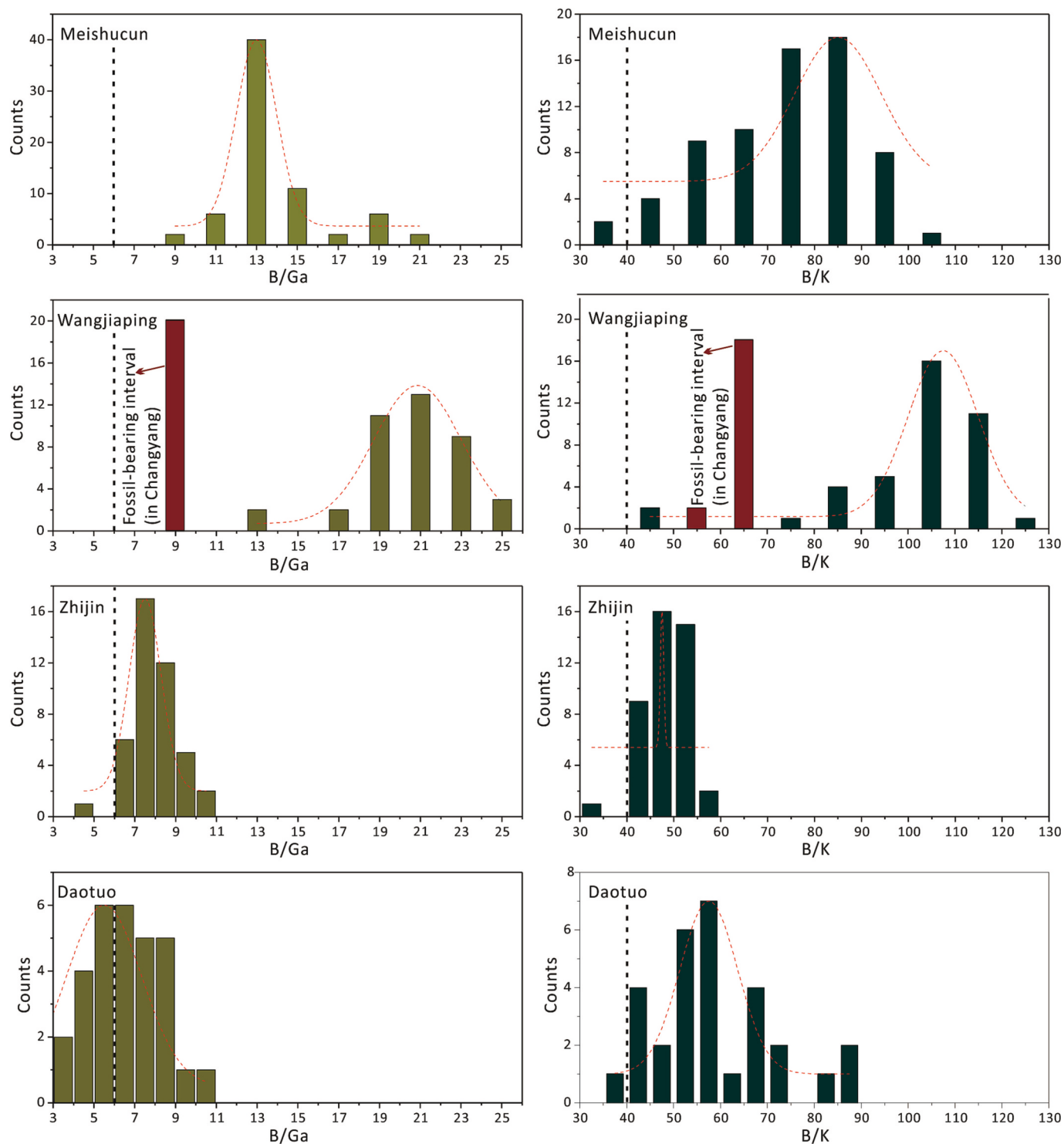
Fig. 5. Frequency distribution histogram of the B/Ga and B/K ratios in the studied section. The black dashed lines denote the marine and non-marine salinity thresholds (B/Ga = 6; and B/K = 40).

samples did not exhibit significant post-depositional alterations and thus can be employed as effective paleosalinity proxies.

4.2. Possible controls of paleosalinity variations in a marginal basin

Despite that the Nanhua Basin may have evolved into fully marine environments since the late Neoproterozoic (Yang et al., 2020), secular variations in watermass salinity are possible considering its marginal location with respect to the open ocean (Cheng et al., 2023). The

watermass salinity in a marginal basin is generally determined by the hydrological balance (precipitation and runoff versus evaporation) and the watermass exchange with the open ocean (Algeo et al., 2008; Gilleaudeau et al., 2021; Huang et al., 2021). A negative hydrological balance (evaporation exceeds precipitation and runoff) can increase the watermass salinity, whereas the watermass salinity decreases when precipitation and runoff exceed evaporation (Huang et al., 2021). In addition, salinity changes during the watermass exchange with the open ocean depend on the relative salinity gradient (Huang et al., 2021;
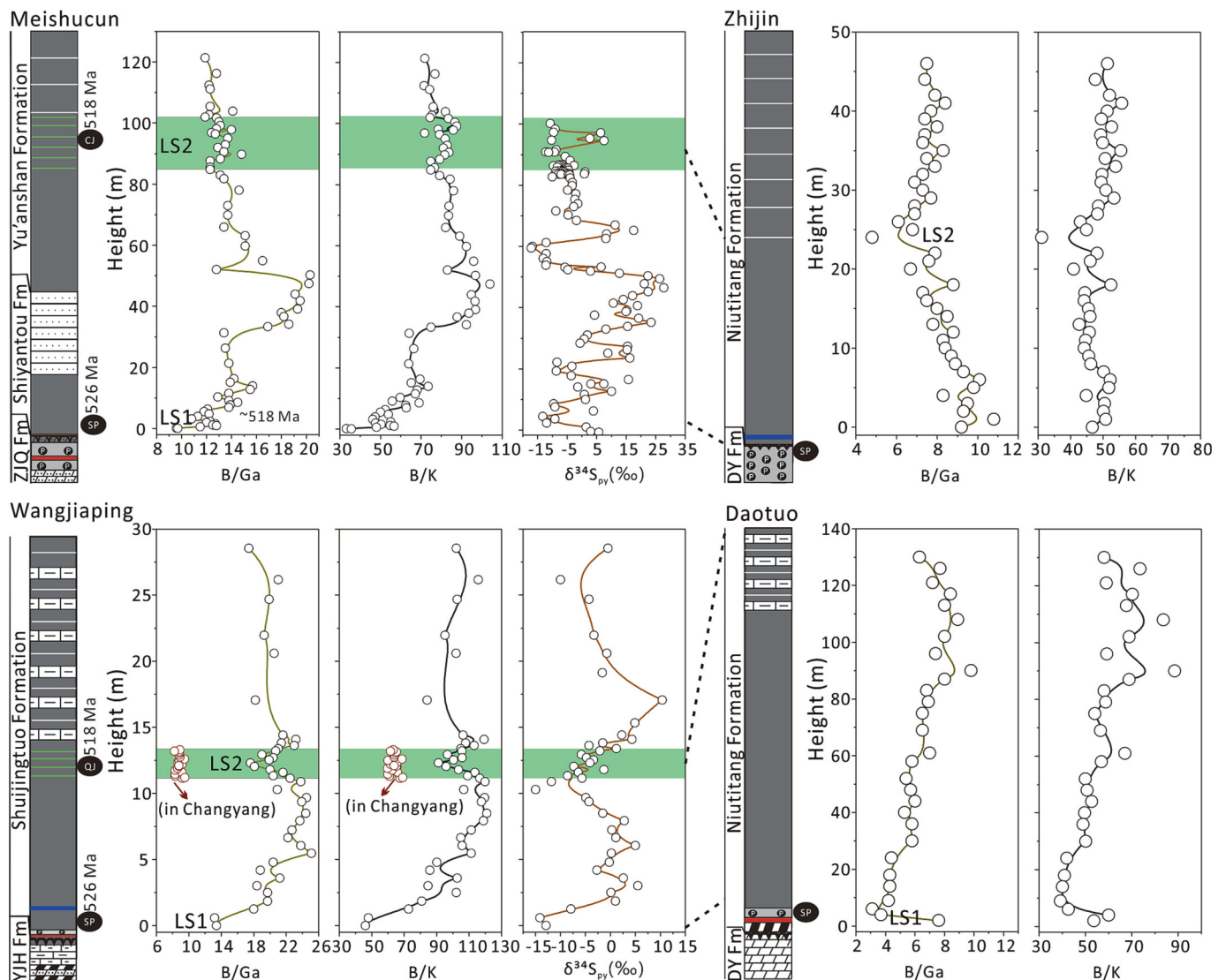
Fig. 6. Evolution of the B/Ga and B/K ratios and $\delta^{34}S_{py}$ values in the studied sections. The $\delta^{34}S_{py}$ values of the Qiongzhushi Formation were cited from the nearby CJ1 drill-core (background sediments; Hammarlund et al., 2017) and normalized based on the fossiliferous position. LS1 (~526 Ma) and LS2 (~518 Ma) are the two relatively low-salinity intervals. Note that only the studied interval of the section (see Fig. 1) was shown in Fig. 6.

Kontakiotis et al., 2022). Generally, marginal basins develop a slightly lower salinity than the open ocean owing to effective freshwater input; therefore, basin salinity could be increased during enhanced watermass exchange with the open ocean (Gilleaudeau et al., 2021; Wei et al., 2022). However, hypersaline watermass could be developed in strictly restricted marginal basins resulting from strong evaporation; examples include the modern Red Sea and Dead Sea (Reiss et al., 2021) and the Messinian Mediterranean (Kontakiotis et al., 2022). For a hypersaline marginal basin, we can expect that an abrupt exchange with the open ocean will lower the watermass salinity. Therefore, prior to deciphering paleosalinity changes, overall salinity conditions in the early Cambrian Nanhua Basin should be firstly constrained.

4.3. Spatial paleosalinity variations in the early Cambrian Nanhua Basin

Despite that the B/Ga and B/K ratios are not quantitative paleosalinity proxies, they can be employed as preliminary paleosalinity evaluation based on the modeling results of modern sediments (Retallack, 2020; Wei and Algeo, 2020). Particularly, the B/Ga ratios have been established statistical relationship to watermass salinity and have been widely employed for paleosalinity reconstruction (Wei and Algeo,

2020; Wei et al., 2022; Cheng et al., 2023). In shallow-water regions, the B/Ga and B/K ratios were 13.8 ± 2.3 and 73.5 ± 15.7, respectively, in Meishucun and are 20.6 ± 2.7 and 101.1 ± 17.1, respectively, in Wangjiaping (Table S1), which are much higher than the marine thresholds (B/Ga = 6 and B/K = 40; Retallack, 2020; Wei and Algeo, 2020), likely indicating hypersaline conditions. For example, following the linear relationship between the B/Ga ratio and salinity in modern marine systems (Wei and Algeo, 2020), the B/Ga ratios in Wangjiaping (20.6 ± 2.7) indicated an average salinity of 52‰. The overall salinity in Meishucun was relatively lower than Wangjiaping indicated by the relatively lower B/Ga and B/K ratios (Fig. 5), which may result from more effective freshwater input in Meishucun. This is consistent with paleogeography reconstruction, which suggests that the Chengjiang Biota developed at near-delta environments (Saleh et al., 2022), whereas the Qingjiang Biota inhabited more offshore settings (Fu et al., 2019). Nevertheless, the high-B/Ga endmembers in Meishucun (~20; Fig. 6) are similar to Wangjiaping, indicating at least intermittent hypersaline conditions in Meishucun. Together, the shallow-water salinity is changeable, but hypersaline conditions are likely to be common during most of the period from late Age 2 to Age 3.
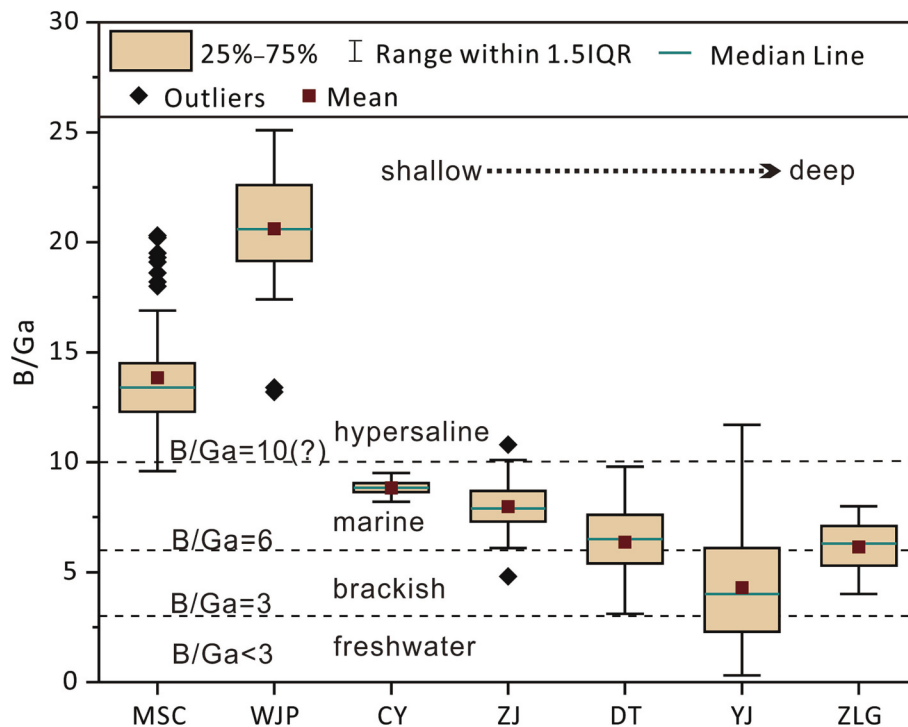
Fig. 7. Box plot of the B/Ga ratio in the studied sections. MSC = Meishucun; WJP = Wangjiaping; JYK = Jinyangkou; ZJ = Zhijin; DT = Daotuo; YJ = Yuanjia (Cheng et al., 2023); ZLG = Zhalagou (Cheng et al., 2023). The MSC, WJP, and CY (relatively deeper) are shallow-water regions, the ZJ and DT are middle-depth water environments, the YJ and ZLG are deep-water environments. Note that the hypersaline B/Ga threshold (~10) has not been precisely defined yet.

In contrast, much lower B/Ga (8.8 ± 0.4) and B/K (64 ± 2.8) ratios were documented within the fossiliferous interval in Jinyangkou (Table S1), which may have much deeper depositional environments than Wangjiaping in Yichang district given that Jinyangkou is located farther away from the Neoproterozoic Huangling anticline (Fig. 1). Similarly, low B/Ga and B/K ratios were also documented at the middle-depth water Zhijin (8.0 ± 1.1 and 48.2 ± 4.5, respectively) and Daotuo locales (6.4 ± 1.6 and 57.6 ± 12.3, respectively) (Figs. 5 and 6; Table S1). These values are close to the marine thresholds (B/Ga = 6 and B/K = 40; Retallack, 2020; Wei and Algeo, 2020), indicating that middle-depth waters were dominated by normal seawater salinity. Recently, Cheng et al. (2023) found that basinal deep waters (Yuanjia and Zhalagou sections) in the Nanhua Basin were dominated by brackish to marine salinity during late Age 2 to Age 3, basically consistent with our observations (Fig. 7). Together, the hypersaline conditions at the shallow-water Meishucun and Wangjiaping locales may be a consequence of a locally negative hydrological balance. Similar hypersaline conditions are common in modern shallow-water lagoons owing to strong evaporation (Shadrin et al., 2019; Lam-Gordillo et al., 2022). During the early Cambrian (late Age 2 to Age 3), the South China Craton was located was located at ~10–20°N paleolatitudes (Fig. 1; Meert and Lieberman, 2008; Zhang et al., 2015). Strong surface evaporation can also be supported by recent paleotemperature reconstructions, which suggest mean surface seawater temperatures can reach 30–38 °C at tropical paleolatitudes during the Cambrian Explosion (Hearing et al., 2018, 2021). If true, our new data revealed that the early Cambrian Nanhua Basin was dominated by brackish to normal seawater salinity, although hypersaline conditions may be typical in shallow-water regions owing to strong evaporation.

4.4. Temporal paleosalinity evolution in the early Cambrian Nanhua Basin

At the shallow-water Meishucun and Wangjiaping locales, the B/Ga and B/K ratios systematically increased in the lower Qiongzhushi (B/Ga

= ~9–20; B/K = ~40–95) and Shuijingtuo (B/Ga = ~14–25; B/K = ~50–120) formations (Fig. 6), indicating a gradual paleosalinity evolution from normal marine to hypersaline conditions from late Age 2 to early Age 3 (~526 to ~518 Ma). During late Age 3 (~518–515 Ma), the B/Ga and B/K ratios systematically decreased in the upper Qiongzhushi and Shuijingtuo formations. Specifically, the B/Ga and B/K ratios quickly decreased by ~7 and ~ 20, respectively, during the intensive explosion of the Chengjiang and Qingjiang biotas at ~518 Ma, which may indicate a quick paleosalinity recovery from hypersalinity to near normal marine salinity at that time (Fig. 6). Indeed, a normal seawater salinity was recorded within the fossiliferous interval in Jinyangkou (deeper than Wangjiaping; Fig. 6). In contrast, the changes in the B/Ga and B/K ratios were relatively moderate in the middle-depth water environments. Nevertheless, the slight but systematic increase in the B/Ga and B/K ratios in the lower Jiumenchong Formation in Daotuo may be comparable to the paleosalinity increase in shallow-water regions from late Age 2 to early Age 3 based on stratigraphic corrections (Figs. 2 and 6). Similarly, Cheng et al. (2023) observed systematic increase in the B/Ga ratio at the deep-water (basinal) Yuanjia and Zhalagou sections in the Nanhua Basin from late Age 2 to early Age 3. Additionally, abrupt decreases in B/Ga and B/K ratios can be identified in the middle Niutitang Formation in Zhijin, which may be equivalent to the paleosalinity decline in shallow-water regions at ~518 Ma (Fig. 6). Therefore, these paleosalinity changes are not local signals but at least basin-scale fluctuations, although the paleosalinity fluctuations in middle- to deep-water environments are relatively moderate.

As constrained in Section 4.2, the early Cambrian Nanhua Basin developed overall brackish to normal seawater conditions with hypersaline conditions only developed in shallow-water regions. Therefore, more effective watermass exchange with the open ocean during transgression would enhance the overall salinity, whereas less effective watermass exchange during regression would lower the overall salinity in the Nanhua Basin. We note that the systematic increase in paleosalinity from late Age 2 to early Age 3 occurred immediately upon a regional unconformity in the early Cambrian Nanhua Basin (Fig. 3;

Jiang et al., 2012), which is globally comparable (Ripperdan, 1994). Therefore, the early sediments upon the regional unconformity must indicate a new-round transgressive event, which may be the major reason for the systematic paleosalinity increase from late Age 2 to early Age 3 (Cheng et al., 2023). Subsequently, a stepwise regression occurred during late Age 3 according to the sea-level reconstruction based on the lithology stratigraphy (Fig. 1; Peng et al., 2020), which may be responsible for the stepwise paleosalinity decline during late Age 3. The sea-level fluctuations may have deep roots in orbitally-paced climate changes (Zhang et al., 2022). Regardless, we have found that the paleosalinity fluctuations in the early Cambrian Nanhua Basin were basically coupled with sea-level changes. Note that brackish B/Ga and B/K ratios (B/Ga < 6 and B/K < 40) occurred in middle-depth water Zhijin and Daotuo locales at ~526 Ma and ~ 518 Ma (Fig. 6), indicating that the overall salinity in the Nanhua Basin may have transiently evolved into brackish conditions. Meanwhile, the shallow-water paleosalinity conditions may have transiently decreased to near-normal seawater salinity levels (Fig. 6; we denote these two relatively low-salinity intervals as LS1 and LS2, respectively, in the following discussion). It is interesting that the LS1 and LS2 may correspond to two sea level lowstands (Fig. 1; Peng et al., 2020). The ~526 Ma sea level lowstands can be most directly supported by the occurrence of the regional unconformity in the early Cambrian Nanhua Basin (Jiang et al., 2012), whereas the ~518 Ma one can be reflected by the increased mudstone and carbonate components (Fu et al., 2019). Therefore, the development of brackish conditions in the Nanhua Basin at ~526 Ma and ~ 518 Ma may result from decreased watermass exchange with the open ocean during sea level lowstands.

Alternatively, the brackish conditions in the Nanhua Basin at LS1 and LS2 may reflect massive fresh-water input (Gilleaudeau et al., 2021; Huang et al., 2021), which can be supported by the pyrite $\delta^{34}S_{py}$ values. The B/Ga and B/K ratios in the Meishucun and Wangjiaping showed very similar evolutionary trends to pyrite $\delta^{34}S_{py}$ values (Fig. 6). For example, LS1 and LS2 were well mirrored by the lowest endmember $\delta^{34}S_{py}$ values (approximately −15‰ to −10‰), indicating similar controlling mechanisms. The $\delta^{34}S_{py}$ values were determined by sulfur isotope compositions of marine sulfate and isotope fractionation during bacterial sulfate reduction (BSR) (Price and Shieh, 1979; Li et al., 2015). Previous studies have confirmed that marine sulfate concentrations were extremely low near the Ediacaran–Cambrian boundary (< 2 mM; Li et al., 2015). In this situation, the sulfur isotope composition of marine sulfate could be readily changed; therefore, the low endmember $\delta^{34}S_{py}$ values may reflect an increased input of isotopically light riverine sulfate, as proposed in early studies (Li et al., 2015; Feng et al., 2014). Alternatively, the low endmember $\delta^{34}S_{py}$ values could be interpreted as an increased sulfate availability because a high sulfate availability could greatly enhance sulfur isotope fractionation during BSR (Price and Shieh, 1979; Zhang et al., 2018). Importantly, terrigenous runoff is the major input pathway of sulfate into the Nanhua Basin; thus, a high sulfate availability also indicates an effective freshwater input. Together, the low endmember $\delta^{34}S_{py}$ values may reflect massive freshwater input into the Nanhua Basin at ~526 Ma and ~ 518 Ma, which may be the major reason for both LS1 and LS2.

### 4.5. Implications for the Cambrian Explosion

Dissolved oxygen is essential for skeletonized metazoans to maintain their basic metabolic activity (Graham et al., 1995); therefore, previous studies have mainly focused on paleoredox research and have proposed that coupled oceanic oxygenation (Chen et al., 2015b; Li et al., 2017) or redox fluctuations (Wei et al., 2020) may have stimulated the Cambrian Explosion. An important finding of these works is that the early Cambrian Nanhua Basin was characterized by highly heterogeneous redox conditions along the water-depth gradient. Specifically, shallow water was oxic, below which water columns were dominated by ferruginous conditions with a dynamic euxinic watermass at middle-depth locations (Jin et al., 2016; Li et al., 2017). As a consequence, middle-

to deep-water environments are generally absent of important fossil records, but some hypoxia-tolerant sponge faunas were found in lower Niutitang Formation termed as the Niutitang Sponge Fauna (Steiner et al., 1993). Additionally, anoxic conditions may have transiently expanded into shallow-water regions during late Age 2 (~525 Ma; Wei et al., 2020). Similarly, the equivalent Niutitang Sponge Fauna has been reported in basal Qiongzhusi (lower part in Shiyantou Member) and Shuijingtuo formations (Steiner et al., 2007; Liu et al., 2022) in shallow-water regions. We need to point out that Nanhua Basin shallow-water regions were dominated by relatively stable oxic conditions after the late Age 2 anoxic event (Chen et al., 2015b). However, above the Niutitang Sponge Fauna, there is a long-term poorly fossiliferous zone in the early Cambrian Nanhua Basin until the occurrences of the Burgess Shale-type Chengjiang and Qingjiang biotas in shallow-water regions (~518 Ma; Yang et al., 2018). Both the Chengjiang and Qingjiang biotas contain >100 taxa, mainly including arthropods (trilobites), sponges, brachiopods, and some tentative echinoderms (Steiner et al., 2005; Fu et al., 2019), which are typical marine fossils. As discussed in Section 4.2, hypersaline conditions may be common in the Nanhua Basin shallow-water regions from late Age 2 to Age 3 (Fig. 8). Therefore, although shallow waters have adequate oxygen for early metazoans, the hypersaline conditions in these regions may have functioned as a critical physiological barrier to metazoan diversification. On the other hand, although middle- to deep-water environments have suitable salinity conditions (Fig. 8), prevailing anoxic and even sulfidic conditions were also fatal to metazoans. Therefore, these observations may indicate that oxygen is not a unique control on early Cambrian biological evolution, salinity environments may also be critical.

Notably, shallow waters may have transiently maintained near-normal seawater salinity at ~526 Ma (LS1) and ~ 518 Ma (LS2), during which the salinity barrier may have been basically removed. However, anoxic conditions may have transiently expanded into shallow-water regions at ~525 Ma (Wei et al., 2020). Therefore, only large amounts of hypoxia-tolerant sponge fauna occurred during LS1 (Yang et al., 2004; Xiao et al., 2005; Steiner et al., 2007), indicating oxygen level control on metazoan diversification. On the other hand, although oxic shallow waters may have been quickly recovered at ~521 Ma (Chen et al., 2015b), no important fossils occurred within the high-salinity interval between LS1 and LS2, suggesting hypersalinity restriction on metazoan diversification. Instead, when the salinity in shallow waters was recovered to near-normal seawater levels at ~518 Ma (LS2), the Chengjiang and Qingjiang biotas were intensively exploded (Steiner et al., 2005; Fu et al., 2019). Additionally, in Yichang district, we note that the paleosalinity within the Qingjiang Biota interval in Jinyangkou was lower than that in Wangjiaping owing to the relatively deeper depositional environments (Figs. 5 and 6). Consequently, Jinyangkou has been reported to contain the most abundant Qingjiang fossil assemblages in Yichang district (Fu et al., 2019). These observations indicate that salinity controlled early Cambrian metazoan evolution and diversification. In summary, although shallow-water regions were dominated by hypersaline conditions from late Age 2 to Age 3, the transient salinity decline driven by an increased freshwater input may have provided inhabitable salinity environments for the Cambrian Explosion.

5. Conclusions

Four spatially comparative sections from late Age 2 to Age 3 (~526–515 Ma) were analyzed with the B/Ga and B/K ratios to constrain paleosalinity conditions and their links to the Cambrian Explosion in the Nanhua Basin. The new data revealed that hypersaline conditions were common in shallow-water regions, whereas middle-depth waters were characterized by normal seawater salinity. Nevertheless, two low-salinity intervals developed at ~526 Ma (LS1) and ~ 518 Ma (LS2), during which the shallow-water salinity may approach that of normal seawater owing to the massive freshwater input into the
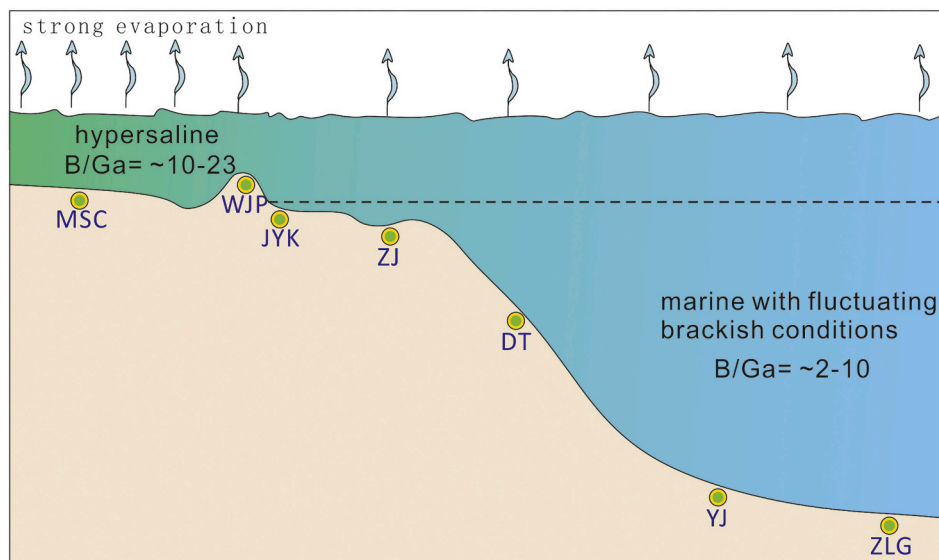
Fig. 8. Salinity pattern of the early Cambrian Nanhua Basin, indicating that hypersaline conditions are common in the shallow-water environments, whereas the middle- to deep-water environments are marked by normal marine salinity with fluctuating brackish conditions. MSC = Meishucun; WJP = Wangjiaping; JYK = Jinyangkou; ZJ = Zhijin; DT = Daotuo; YJ = Yuanjia (Cheng et al., 2023); ZLG = Zhalagou (Cheng et al., 2023).

Nanhua Basin at that time. Importantly, LS1 and LS2 may have provided transient inhabitable salinity environments for early metazoan evolution. During LS1, metazoan diversification was restricted by transient shallow-water anoxia, but large amounts of hypoxia-tolerant sponges occurred. Instead, the Chengjiang and Qingjiang biotas experienced intense explosion during LS2 (~518 Ma) in oxic shallow-water environments. However, within the hypersalinity interval between LS1 and LS2, no important faunas occurred, although shallow-water regions were oxic. Together, paleosalinity may have critically controlled metazoan evolution during the early Cambrian, although more investigation is needed.

Declaration of Competing Interest

The authors declare that they have no known competing financial interests or personal relationships that could have appeared to influence the work reported in this paper.

Data availability

Data were included in the supplementary material.

Appendix A. Supplementary data

Supplementary data to this article can be found online at https://doi.org/10.1016/j.palaeo.2023.111716.

References

Algeo, T.J., Heckel, P.H., Maynard, J.B., Blakey, R., Rowe, H., Pratt, B.R., Holmden, C., 2008. Modern and ancient epeiric seas and the super-estuarine circulation model of marine anoxia. In: Dynamics of Epeiric Seas: Sedimentological, Paleontological and Geochemical Perspectives, 48. Geological Association of Canada, St. John's, Canada, pp. 7–38. Special Publication.

Chen, D., Zhou, X., Fu, Y., Wang, J., Yan, D., 2015. New U-Pb zircon ages of the Ediacaran-Cambrian boundary strata in South China. Terra Nova 27, 62–68.

Chen, X., Ling, H., Vance, D., Shields-Zhou, G.A., Zhu, M., Poulton, S.W., Och, L.M., Jiang, S., Li, D., Cremonese, L., Archer, C., 2015. Rise to modern levels of ocean oxygenation coincided with the Cambrian radiation of animals. Nat. Commun. 6, 7142.

Cheng, M., Zhang, Z., Jin, C., Wei, W., Wang, H., Algeo, T.J., Li, C., 2023. Salinity variation and hydrolographic dynamics in the early Cambrian Nanhua Basin (South China). Sci. China: Earth Sci. 66, 1674–7313.

Clift, P.D., Wan, S., Blusztajn, J., 2014. Reconstructing chemical weathering, physical erosion and monsoon intensity since 25 Ma in the northern South China Sea: a review of competing proxies. Earth-Sci. Rev. 130, 86–102.

Compston, W., Zhang, Z., Cooper, J.A., Ma, G., Jenkins, R.J.F., 2008. Further SHRIMP geochronology on the early Cambrian of South China. Am. J. Sci. 308, 399–420.

Feng, L., Li, C., Huang, J., Chang, H., Chu, X., 2014. A sulfate control on marine mid-depth euxinia on the early Cambrian (ca. 529–521Ma) Yangtze platform, South China. Precambrian Res. 246, 123–133.

Frederickson, A.F., Reynolds, J., 1960. Geochemical method for determining paleosalinity. Clay Clay Miner. 8, 203–213.

Fu, D., Tong, G., Dai, T., Liu, W., Yang, Y., Zhang, Y., Cui, L., Li, L., Yun, H., Wu, Y., Sun, A., Liu, C., Pei, W., Gaines, R.R., Zhang, X., 2019. The Qingjiang biota—A Burgess Shale–type fossil Lagerstätte from the early Cambrian of South China. Science 363, 1338–1342.

Gilleaudeau, G.J., Algeo, T.J., Lyons, T.W., Bates, S., Anbar, A.D., 2021. Novel watermass reconstruction in the early Mississippian Appalachian Seaway based on integrated proxy records of redox and salinity. Earth Planet. Sci. Lett. 558, 116746.

Graham, J.B., Dudley, R., Aguilar, N.M., Gans, C., 1995. Implications of the late Palaeozoic oxygen pulse for physiology and evolution. Nature 375, 117–120.

Guilbaud, R., Slater, B.J., Poulton, S.W., Harvey, T.H.P., Brocks, J.J., Nettersheim, B.J., Butterfield, N.J., 2018. Oxygen minimum zones in the early Cambrian Ocean. Geochem. Perspect. Lett. 6, 33–38.

Hammarlund, E.U., Gaines, R.R., Prokopenko, M.G., Qi, C., Hou, X., Canfield, D.E., 2017. Early Cambrian oxygen minimum zone-like conditions at Chengjiang. Earth Planet. Sci. Lett. 475, 160–168.

Hay, W.W., Migdisov, A., Balukhovsky, A.N., Wold, C.N., Flögel, S., Söding, E., 2006. Evaporites and the salinity of the ocean during the Phanerozoic: Implications for climate, ocean circulation and life. Palaeogeogr., Palaeoclimatol., Palaeoecol. 240, 3–46.

Hearing, T.W., Harvey, T.H.P., Williams, M., Leng, M.J., Lamb, A.L., Wilby, P.R., Gabbott, S.E., Pohl, A., Donnadieu, Y., 2018. An early Cambrian greenhouse climate. Sci. Adv. 4, eaar5690.

Hearing, T.W.W., Pohl, A., Williams, M., Donnadieu, Y., Harvey, T.H.P., Scotese, C.R., Sepulchre, P., Franc, A., Vandenbroucke, T.R.A., 2021. Quantitative comparison of geological data and model simulations constrains early Cambrian geography and climate. Nat. Commun. 12 (2021), 3868.

Henry, R.P., Lucu, Č., Onken, H., Weihrauch, D., 2012. Multiple functions of the crustacean gill: osmotic/ionic regulation, acid-base balance, ammonia excretion, and bioaccumulation of toxic metals. Front. Physiol. 3, 431.

Hrstka, T., Gottlieb, P., Skala, R., Breiter, K., Motl, D., 2018. Automated mineralogy and petrology-applications of TESCAN Integrated Mineral Analyzer (TIMA). J. Geosci. 63, 47–63.

Huang, T., Chen, D., Fu, Y., Yeasmin, R., Guo, C., 2019. Development and evolution of a euxinic wedge on the ferruginous outer shelf of the early Cambrian Yangtze Sea. Chem. Geol. 524, 259–271.

Huang, Y., Zheng, Y., Heng, P., Giosan, L., Coolen, M.J.L., 2021. Black Sea paleosalinity evolution since the last deglaciation reconstructed from alkenone-inferred Isochrysidales diversity. Earth Planet. Sci. Lett. 564, 116881.

Jewuła, K., Środoń, J., Kuligiewicz, A., Mikołajczak, M., Liivamägi, S., 2022. Critical evaluation of geochemical indices of palaeosalinity involving boron. Geochim. Cosmochim. Acta 322, 1–23.

Jiang, G., Wang, X., Shi, X., Xiao, S., Zhang, S., Dong, J., 2012. The origin of decoupled carbonate and organic carbon isotope signatures in the early Cambrian (ca. 542–520Ma) Yangtze platform. Earth Planet. Sci. Lett. 317–318, 96–110.

Jin, C.S., Li, C., Algeo, T.J., Planavsky, N.J., Cui, H., Yang, X.L., Zhao, Y.L., Zhang, X.L., Xie, S.C., 2016. A highly redox-heterogeneous ocean in South China during the early Cambrian (~529-514 Ma): Implications for biota-environment coevolution. Earth Planet. Sci. Lett. 441, 38–51.

Knauth, L.P., 2005. Temperature and salinity history of the Precambrian ocean: implications for the course of microbial evolution. Palaeogeogr., Palaeoclimatol., Palaeoecol. 219, 53–69.

Kontakiotis, G., Butiseacă, G.A., Antonarakou, A., Agiadi, K., Zarkogiannis, S.D., Krsnik, E., Besiou, E., Zachariasse, W.J., Lourens, L., Thivaiou, D., Koskeridou, E., Moissette, P., Mulch, A., Karakitsios, V., Vasiliev, I., 2022. Hypersalinity accompanies tectonic restriction in the eastern Mediterranean prior to the Messinian Salinity Crisis. Palaeogeogr. Palaeoclimatol. Palaeoecol. 592, 110903.

Krause, A.J., Mills, B.J.W., Zhang, S., Planavsky, N.J., Lenton, T.M., Poulton, S.W., 2018. Stepwise oxygenation of the Paleozoic atmosphere. Nat. Commun. 9 (2018), 4081.

Lam-Gordillo, O., Mosley, L.M., Simpson, S.L., Welsh, D.T., Dittmann, S., 2022. Loss of benthic macrofauna functional traits correlates with changes in sediment biogeochemistry along an extreme salinity gradient in the Coorong lagoon, Australia. Mar. Pollut. Bull. 174, 113202.

Li, C., Cheng, M., Algeo, T.J., Xie, S., 2015. A theoretical prediction of chemical zonation in early oceans (>520 Ma). Sci. China Earth Sci. 58 (11), 1901–1909.

Li, C., Jin, C., Planavsky, N.J., Algeo, T.J., Cheng, M., Yang, X., Zhao, Y., Xie, S., 2017. Coupled oceanic oxygenation and metazoan diversification during the early–middle Cambrian? Geology 45, 743–746.

Liu, Y., Ding, W., Lang, X., Xing, C., Wang, R., Huang, K., Fu, B., Ma, H., Peng, Y., Shen, B., 2022. Refining the early Cambrian marine redox profile by using pyrite sulfur and iron isotopes. Glob. Planet. Chang. 213, 103817.

McLennan, S.M., 2001. Relationships between the trace element composition of sedimentary rocks and upper continental crust. Geochem. Geophys. Geosyst. 2, 203–236.

Meert, J.G., Lieberman, B.S., 2008. The Neoproterozoic assembly of Gondwana and its relationship to the Ediacaran-Cambrian radiation. Gondwana Res. 14, 5–21.

Moran, A.E., Sisson, V.B., Leeman, W.P., 1992. Boron depletion during progressive metamorphism: Implications for subduction processes. Earth Planet. Sci. Lett. 111, 331–349.

Okada, Y., Sawaki, Y., Komiya, T., Hirata, T., Takahata, N., Sano, Y., Han, J., Maruyama, S., 2014. New chronological constraints for Cryogenian to Cambrian rocks in the Three Gorges, Weng'an and Chengjiang areas, South China. Gondwana Res. 25, 1027–1044.

Peng, S.C., Babcock, L.E., Ahlberg, P., 2020. Chapter 19-The Cambrian Period. In: Gradstein, F.M., et al. (Eds.), Geologic Time Scale 2020. Elsevier, Amsterdam, pp. 565–629. https://doi.org/10.1016/B978-0-12-824360-2.00019-X.

Price, F.T., Shieh, Y.N., 1979. Fractionation of sulfur isotopes during laboratory synthesis of pyrite at low temperatures. Chem. Geol. 27, 245–253.

Reinhard, C.T., Planavsky, N.J., Gill, B.C., Ozaki, K., Robbins, L.J., Lyons, T.W., Fischer, W.W., Wang, C., Cole, D.B., Konhauser, K.O., 2017. Evolution of the global phosphorus cycle. Nature 541, 386–389.

Reiss, A.G., Ganor, J., Hamawi, M., Gavrieli, I., 2021. Dynamics of turbidity in gypsum-precipitating brines: the case of the Red Sea-Dead Sea project. J. Environ. Manag. 288, 112369.

Remírez, M.N., Algeo, T.J., 2020. Paleosalinity determination in ancient epicontinental seas: a case study of the T-OAE in the Cleveland Basin (UK). Earth-Sci. Rev. 201, 103072.

Retallack, G., 2020. Boron paleosalinity proxy for deeply buried Paleozoic and Ediacaran fossils. Palaeogeogr. Palaeoclimatol. Palaeoecol. 540, 109536.

Richardson, J.B., Mischenko, I.C., Mackowiak, T.J., Perdrial, N., 2022. Trace metals and metalloids and Ga/Al ratios in grey shale weathering profiles along a climate gradient and in batch reactors. Geoderma 405, 115431.

Ripperdan, R.L., 1994. Global variations in carbon isotope composition during the latest Neoproterozoic and earliest Cambrian. Annu. Rev. Earth Planet. Sci. 22, 385–417.

Saleh, F., Qi, C., Buatois, L.A., Mángano, M.G., Paz, M., Vaucher, R., Zheng, Q., Hou, X., Gabbott, S.E., Ma, X., 2022. The Chengjiang Biota inhabited a deltaic environment. Nat. Commun. 13, 1569.

Shadrin, N., Kolesnikova, E., Revkova, T., Latushkin, A., Chepyzhenko, A., Dyakov, N., Anufriieva, E., 2019. Macrostructure of benthos along a salinity gradient: the case of

Sivash Bay (the Sea of Azov), the largest hypersaline lagoon worldwide. J. Sea Res. 154, 101811.

Shore, A.J., Wood, R.A., Butler, I.B., Zhuravlev, A.Y., McMahon, S., Curtis, A., Bowyer, F. T., 2021. Ediacaran metazoan reveals lophotrochozoan affinity and deepens root of Cambrian Explosion. Sci. Adv. 7, eabf2933.

Sperling, E.A., Wolock, C.J., Morgan, A.S., Gill, B.C., Kunzmann, M., Halverson, G.P., Macdonald, F.A., Knoll, A.H., Johnston, D.T., 2015. Statistical analysis of iron geochemical data suggests limited late Proterozoic oxygenation. Nature 523, 451–454.

Srodon, J., 2010. Evolution of boron and nitrogen content during illitization of bentonites. Clay Clay Miner. 58, 743–756.

Środoń, J., Paszkowski, M., 2011. Role of clays in the diagenetic history of nitrogen and boron in the Carboniferous of Donbas (Ukraine). Clay Miner. 46, 561–582.

Steiner, M., Mehl, D., Reitner, J., Erdtmann, B.-D., 1993. Oldest entirely preserved sponges and other fossils from the Lowermost Cambrian and a new facies reconstruction of the Yangtze platform (China). Berl. Geowiss. Abh., E Palaobiol. 9, 293–329.

Steiner, M., Zhu, M., Zhao, Y., Erdtmann, B., 2005. Lower Cambrian Burgess Shale-type fossil associations of South China. Palaeogeogr., Palaeoclimatol., Palaeoecol. 220, 129–152.

Steiner, M., Li, G., Qian, Y., Zhu, M., Erdtmann, B., 2007. Neoproterozoic to Early Cambrian small shelly fossil assemblages and a revised biostratigraphic correlation of the Yangtze Platform (China). Palaeogeogr., Palaeoclimatol., Palaeoecol. 254, 67–99.

Walker, C.T., 1968. Evaluation of boron as a paleosalinity indicator and its application to offshore prospects. AAPG Bull. 52, 751–766.

Wei, G., Planavsky, N.J., Tarhan, L.G., He, T., Wang, D., Shields, G.A., Wei, W., Ling, H., 2020. Highly dynamic marine redox state through the Cambrian explosion highlighted by authigenic δ238U records. Earth Planet. Sci. Lett. 544, 116361.

Wei, W., Algeo, T.J., 2020. Elemental proxies for paleosalinity analysis of ancient shales and mudrocks. Geochim. Cosmochim. Acta 287, 341–366.

Wei, W., Yu, W., Algeo, T.J., Herrmann, A.D., Zhou, L., Liu, J., Wang, Q., Du, Y., 2022. Boron proxies record paleosalinity variation in the north American Midcontinent Sea in response to Carboniferous glacio-eustasy. Geology 50, 537–541.

Winter, A., Almogi-Labin, A., Erez, Y., Halicz, E., Luz, B., Reiss, Z., 1983. Salinity tolerance or marine organisms deduced from Red Sea Quaternary record. Mar. Geol. 53, M17–M22.

Xiao, S., Hu, J., Yuan, X., Parsley, R.L., Cao, R., 2005. Articulated sponges from the lower Cambrian Hetang Formation in southern Anhui, South China: their age and implications for the early evolution of sponges. Palaeogeogr. Palaeoclimatol. Palaeoecol. 220, 89–117.

Xu, L.G., Lehmann, B., Mao, J., Qu, W., Du, A., 2011. Re-Os age of polymetallic Ni-Mo-PGE-Au mineralization in early Cambrian Black Shales of South China—a reassessment. Econ. Geol. 106, 511–522.

Yang, F., Zhou, X., Peng, Y., Song, B., Kou, X., 2020. Evolution of Neoproterozoic basins within the Yangtze Craton and its significance for oil and gas exploration in South China: an overview. Precambrian Res. 337, 105563.

Yang, R., Qian, Y., Zhang, J., Zhang, W., Jiang, L., Gao, H., 2004. Sponge spicules in phosphorites of the Early Cambrian Gezhongwu Formation, Zhijin, Guizhou. Prog. Nat. Sci. 14, 896–902.

Yang, Y., Zhang, X., Liu, S., Zhou, T., Fan, H., Yu, H., Cheng, W., Huang, F., 2018. Calibrating NIST SRM 683 as a new international reference standard for Zn isotopes. J. Anal. At. Spectrom. 33, 1777–1783.

Ye, C., Yang, Y., Fang, X., Zhang, W., 2016. Late Eocene clay boron-derived paleosalinity in the Qaidam Basin and its implications for regional tectonics and climate. Sediment. Geol. 346, 49–59.

You, C.F., Chan, L.H., Spivack, A.J., Gieskes, J.M., 1995. Lithium, boron, and their isotopes in sediments and pore waters of Ocean Drilling Program Site 808, Nankai Trough: implications for fluid expulsion in accretionary prisms. Geology 23, 37–40.

Zhang, S., Li, H., Jiang, G., Evans, D.A.D., Dong, J., Wu, H., Yang, T., Liu, P., Xiao, Q., 2015. New paleomagnetic results from the Ediacaran Doushantuo Formation in South China and their paleogeographic implications. Precambrian Res. 259, 130–142.

Zhang, T., Li, Y., Fan, T., Da Silva, A., Shi, J., Gao, Q., Kuang, M., Liu, W., Gao, Z., Li, M., 2022. Orbitally-paced climate change in the early Cambrian and its implications for the history of the Solar System. Earth Planet. Sci. Lett. 583, 117420.

Zhang, T., Zhang, Q., Qu, Y., Wang, X., Zhao, J., 2021. Chapter 5—Interactive effects of ocean acidification and other environmental factors on marine organisms. In: Liu, G. X. (Ed.), Ocean Acidification and Marine Wildlife: Physiological and Behavioral Impacts. Academic Press, pp. 193–246. https://doi.org/10.1016/B978-0-12-822330-7.00001-0.

Zhang, Z., Li, C., Cheng, M., Algeo, T.J., Jin, C., Tang, F., Huang, J., 2018. Evidence for highly complex redox conditions and strong water-column stratification in an early Cambrian continental-margin sea. Geochem. Geophys. Geosyst. 19, 2397–2410.

Zhu, M., Zhang, J., Steiner, M., Yang, A., Li, G., Erdtmann, B., 2003. Sinian-Cambrian stratigraphic framework for shallow- to deep-water environments of the Yangtze Platform: an integrated approach. Prog. Nat. Sci. 13, 951–960.

Zhuravlev, A.Y., Mitchell, E.G., Bowyer, F., Wood, R., Penny, A., 2022. Increases in reef size, habitat and metacommunity complexity associated with Cambrian radiation oxygenation pulses. Nat. Commun. 13 (2022), 7523.